

## Full length article

# Multi-scale and spatially resolved hydrogen mapping in a Ni–Nb model alloy reveals the role of the $\delta$ phase in hydrogen embrittlement of alloy 718



Z. Tarzimoghadam<sup>a</sup>, M. Rohwerder<sup>a</sup>, S.V. Merzlikin<sup>a</sup>, A. Bashir<sup>a</sup>, L. Yedra<sup>b</sup>, S. Eswara<sup>b</sup>, D. Ponge<sup>a,\*</sup>, D. Raabe<sup>a</sup>

<sup>a</sup> Max-Planck-Institut für Eisenforschung GmbH, Max-Planck-Straße 1, 40237 Düsseldorf, Germany

<sup>b</sup> Advanced Instrumentation for Ion-Nano-Analytics (AINA), MRT Department, Luxembourg Institute of Science and Technology (LIST), 41 rue du Brill, 4422 Belvaux, Luxembourg

## ARTICLE INFO

## Article history:

Received 2 December 2015

Received in revised form

12 February 2016

Accepted 22 February 2016

Available online 5 March 2016

## Keywords:

Hydrogen embrittlement

Hydrogen mapping

Alloy 718

Delta phase

HEDE

## ABSTRACT

We investigated the hydrogen distribution and desorption behavior in an electrochemically hydrogen-charged binary Ni–Nb model alloy to study the role of  $\delta$  phase in hydrogen embrittlement of alloy 718. We focus on two aspects, namely, (1) mapping the hydrogen distribution with spatial resolution enabling the observation of the relations between desorption profiles and desorption sites; and (2) correlating these observations with mechanical testing results to reveal the degradation mechanisms. The trapping states of hydrogen in the alloy were globally analyzed by Thermal Desorption Spectroscopy (TDS). Additionally, spatially resolved hydrogen mapping was conducted using silver decoration, Scanning Kelvin Probe Force Microscopy (SKPFM) and Secondary Ion Mass Spectrometry (SIMS): The Ag decoration method revealed rapid effusion of hydrogen at room temperature from the  $\gamma$ -matrix. The corresponding kinetics was resolved in both, space and time by the SKPFM measurements. At room temperature the hydrogen release from the  $\gamma$ -matrix steadily decreased until about 100 h and then was taken over by the  $\delta$  phase from which the hydrogen was released much slower. For avoiding misinterpretation of hydrogen signals stemming from environmental effects we also charged specimens with deuterium. The deuterium distribution in the microstructure was studied by SIMS. The combined results reveal that hydrogen dissolves more preferably inside the  $\gamma$ -matrix and is diffusible at room temperature while the  $\delta$  phase acts as a deeper trapping site for hydrogen. With this joint and spatially resolving approach we observed the microstructure- and time-dependent distribution and release rate of hydrogen with high spatial and temporal resolution. Correlating the obtained results with mechanical testing of the hydrogen-charged samples shows that hydrogen enhanced decohesion (HEDE) occurring at the  $\delta$ /matrix interfaces promotes the embrittlement.

© 2016 Acta Materialia Inc. Published by Elsevier Ltd. All rights reserved.

## 1. Introduction

Alloy 718 is a nickel based superalloy with niobium (Nb) as the major alloying element for precipitation hardening.  $\gamma''$ -Ni<sub>3</sub>Nb, a body centered tetragonal (BCT) ordered compound with D0<sub>22</sub> crystal structure, is the primary strengthening phase in this alloy, interacting with lattice dislocations through coherency strains. The alloy is also susceptible to the formation of orthorhombic  $\delta$ -Ni<sub>3</sub>Nb

(D0<sub>a</sub> crystal structure), which is invariably incoherent with the  $\gamma$ -matrix and does not contribute much to strengthening even when present in significant fractions. The characteristics of  $\delta$  phase formation depend strongly on temperature and it nucleates primarily at  $\gamma$ -grain boundaries [1]. Wide application of alloy 718 in hydrogen containing atmospheres such as sour gas environments when tapping oilfields motivate investigations on the susceptibility of this alloy to hydrogen embrittlement (HE). Recent studies [2–5] attempting to investigate the role of precipitates in HE of alloy 718 have revealed that both, the  $\delta$  and the  $\gamma''$  phases play significant roles in altering HE sensitivity. Specifically the  $\delta$  phase has been suggested to promote HE by initializing micro-cracks, hence a  $\delta$ -

\* Corresponding author.

E-mail address: [ponge@mpie.de](mailto:ponge@mpie.de) (D. Ponge).

free aged alloy was proposed for applications with high hydrogen exposure [3]. However, the real mechanism of the  $\delta$  phase in promoting HE is not yet understood.

A difficulty in explaining the mechanisms of HE concerns the spatially and temporally resolved detection of hydrogen or deuterium. Visualization of hydrogen is essential for revealing its local distribution with respect to its possible preference to trap at certain phases or lattice defects. However, the very low detection sensitivity, high mobility and very low concentration of hydrogen and the limited availability of tools for spatially resolving detection render this field challenging [6]. Several methods have been proposed for direct visualization of hydrogen and/or its isotopes in metallic microstructures, such as silver decoration [7], Hydrogen Microprint Technique (HMT) [8–10], tritium autoradiography [10,11], Secondary Ion Mass Spectrometry (SIMS) [12–15], Atom Probe Tomography (APT) [15–19], and Scanning Kelvin Probe Force Microscopy (SKPFM) either without a palladium (Pd) detection layer [20,21] or in conjunction with a Pd detection layer [22]. SKPFM without a Pd detection layer allows detection of hydrogen in a material by means of the change of the work function caused by hydrogen entering the oxide at the surface (see discussion in Ref. [22]). However, as it is discussed in [20], oxides are improper as detection layers for direct quantification and reliable differentiation between release rates from different phases, due to the complex dependence of the work function pertaining to the type of the oxides and their corresponding defects.

In this study we used a binary Ni–Nb model alloy to elucidate the role of the  $\delta$ -Ni<sub>3</sub>Nb intermetallic precipitates in the hydrogen absorption/desorption processes with respect to the  $\gamma$ -matrix and further correlated the results with concurrent failure mechanism. Using a model alloy instead of the more complex engineering Ni-based superalloy compound allows us to narrow down the parameters involved in HE to the two phases and the corresponding interfaces involved. The approach of conducting correlative measurements using Thermal Desorption Spectroscopy (TDS), silver decoration, SKPFM in conjunction with a Pd detection layer, and SIMS, enables the identification of hydrogen trapping sites and states in the microstructure. Each individual technique has its advantageous characteristics as well as a specific range of spatial and/or temporal resolution. Combining these allows performing multi-scale mapping of hydrogen in the microstructure, ranging from the macroscale down to few-nanometers. The information obtained by clarifying the behavior of hydrogen desorption, binding energy between the hydrogen and specific trapping sites, and the local hydrogen distribution, are used to discuss the hydrogen assisted failure mechanism in this material.

## 2. Experimental procedures

### 2.1. Material and microstructure characterization

The Ni-22wt-% (15 at.-%) Nb alloy was produced using an electric arc furnace under Ar atmosphere, and cast in a copper mold. Table 1 shows the chemical composition of the as-cast alloy. The as-cast billets were homogenized at 1200 °C for 24 h under Ar atmosphere.

Fig. 1 shows the Ni–Nb binary phase diagram and the composition chosen here. For this composition, the microstructure

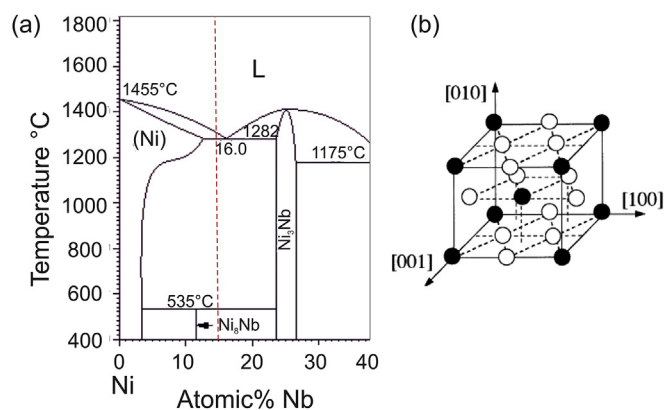


Fig. 1. (a) Ni–Nb binary phase diagram. The composition of the alloy studied here is indicated by the red line. (b) Crystal structure of Ni<sub>3</sub>Nb-DO<sub>a</sub>, with:  $a = 0.5114$  nm,  $b = 0.4244$  nm, and  $c = 0.4538$  nm (at 25 °C) [23,24]. (For interpretation of the references to color in this figure legend, the reader is referred to the web version of this article.)

consists of a  $\gamma$ -matrix (face centered cubic (fcc) structure) consisting of a Ni–Nb solid solution and a  $\delta$ -Ni<sub>3</sub>Nb intermetallic phase (Fig. 1a). Ni<sub>3</sub>Nb-DO<sub>a</sub> ( $\delta$ ) has an orthorhombic structure with eight atoms in the primitive cell ( $Pm\bar{m}n$ , space group 59) (Fig. 1b) [23,24].

Secondary electron (SE) and backscattered electron (BSE) imaging were used for microstructure characterization. Energy-dispersive x-ray spectroscopy (EDX) measurements were carried out to analyze the elemental partitioning. Scanning electron microscopic (SEM) analyses were done in Zeiss–Crossbeam XB 1540 FIB-SEM at 15 kV acceleration voltage. The samples for the SEM observations were prepared by grinding, polishing in diamond suspension and final polishing in colloidal silica suspension.

Fig. 2 shows the microstructure of the alloy. The bright contrasted phase in the light optical micrograph (Fig. 2a) and SE image (Fig. 2b), which reveals the Nb enriched areas in the elemental map (Fig. 2c), corresponds to  $\delta$ -Ni<sub>3</sub>Nb. X-ray diffraction (XRD) analysis<sup>1</sup> also confirmed the presence of the  $\gamma$  and  $\delta$  phases.

Hydrogen was introduced into the specimens with dimensions of 15 mm  $\times$  15 mm  $\times$  1 mm thickness via electrochemical charging for 2 h. A platinum foil with dimensions of 25 mm  $\times$  25 mm  $\times$  0.1 mm thickness was used as the counter electrode. Prior to hydrogen charging, samples were prepared by mechanical polishing with colloidal silica to ensure a deformation-free surface. The sample surface was checked before and after hydrogen charging; no surface defects were caused due to the chosen hydrogen charging conditions.

### 2.2. Thermal Desorption Spectroscopy (TDS)

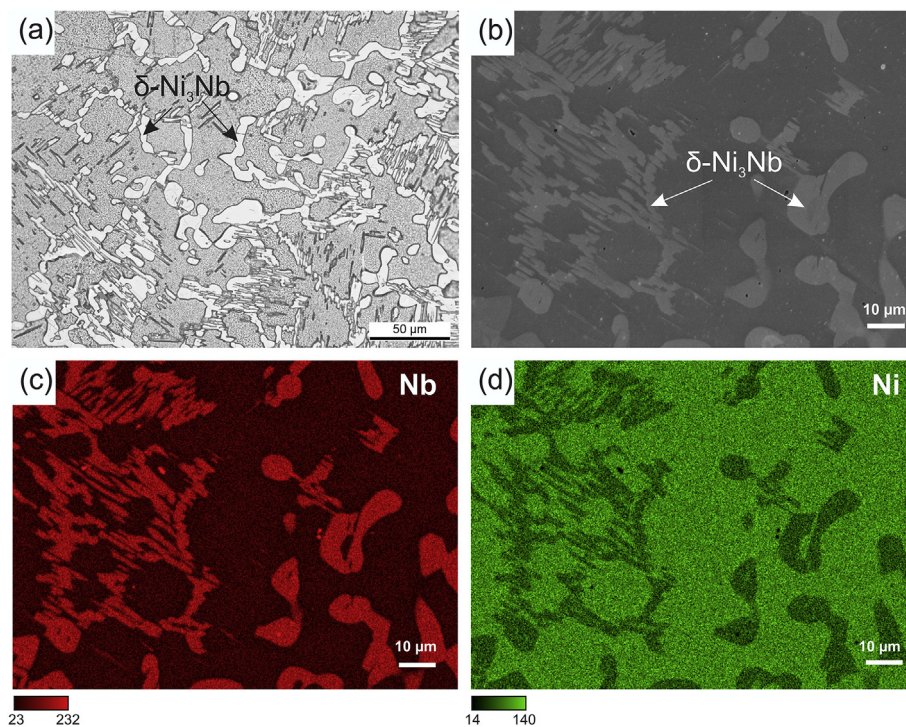
Thermal desorption (TD) experiments were carried out using a custom-designed UHV-based Thermal Desorption Analysis instrument in conjunction with a Mass Spectrometer detector set up (TDA-MS), described in detail elsewhere [25]. Specimens were charged electrochemically for 2 h in 0.1 mol L<sup>-1</sup> NaOH aqueous solution, at constant potential of  $-1$  V SHE.<sup>2</sup> The specimens were then cleaned with polar and non-polar solvents (C<sub>2</sub>H<sub>5</sub>OH and CCl<sub>4</sub>) prior to the measurement to remove the rests of the electrolyte. The base pressure inside the measurement chamber before analysis was lower than  $4 \times 10^{-9}$  mbar; all TD-experiments were performed

Table 1  
Chemical composition of the as cast alloy (wt.-%).

Nb	Ni	O	H	N	C
22.5	Bal.	0.029	0.00043	0.0006	0.0148

<sup>1</sup> XRD conditions: Diffractometer: Philips PW1830, Co K $\alpha$  radiation ( $\lambda = 0.179$  nm) at 40 kV/30 mA, continuous mode, step size:  $\Delta 2\theta = 0.02^\circ$ , count time: 10 s/step.

<sup>2</sup> SHE: standard hydrogen electrode.



**Fig. 2.** Microstructure of the Ni-22wt-%Nb model alloy: (a) Light optical micrograph, (b) SE image, (c) and (d) corresponding Nb and Ni EDX maps, respectively. Each EDX map is color coded by the count frequency of the X-ray signal received by the EDX detector.

within 15 min after hydrogen charging. The TD analyses were conducted from 25 °C to 800 °C to obtain the hydrogen desorption profiles. Constant heating ramps of 26, 20, 13, 10, and 6.5 °C min<sup>-1</sup> were used to assess activation energies of the hydrogen traps.

### 2.3. Silver decoration technique

Specimens were charged with hydrogen in 0.1 mol L<sup>-1</sup> H<sub>2</sub>SO<sub>4</sub> aqueous solution containing 20 mg L<sup>-1</sup> CH<sub>4</sub>N<sub>2</sub>S, at a current density of 10 mA cm<sup>-2</sup> for 2 h and immersed in the silver decoration solution for 1 h at room temperature. In the present study, a 4.3 mmol L<sup>-1</sup> Ag[K(CN)<sub>2</sub>] aqueous solution was used for silver decoration. Samples were rinsed with distilled water and ethanol and dried. The silver-deposited surface was observed by SE imaging and EDX. For comparison between the hydrogen charged and uncharged states, a sample without hydrogen was immersed for the same time (1 h) in the solution.

### 2.4. Scanning Kelvin Probe Force Microscopy (SKPFM)

The SKPFM measurements were carried out on Agilent 5500 SPM. For the SKPFM measurements, the mechanically polished specimen was slightly etched<sup>3</sup> for producing a small topography difference (<0.2 μm) between the two phases, making it easy to distinguish them. Hydrogen was introduced into the freshly etched sample by electrochemical charging in 0.1 mol L<sup>-1</sup> H<sub>2</sub>SO<sub>4</sub> aqueous solution containing 20 mg L<sup>-1</sup> CH<sub>4</sub>N<sub>2</sub>S, at 10 mA cm<sup>-2</sup> current density for 2 h. After hydrogen charging a 100 nm layer of Pd was evaporated at the surface by physical vapor deposition (PVD). The Pd layer acts as a detection layer for the hydrogen (see Ref. [22] and section 3.3). Finally, the sample was transferred through ambient

lab environment to the SKPFM, where all the measurements were carried out in a dry nitrogen saturated environment to avoid further loss of hydrogen by reaction with oxygen. It took about 4 h from the hydrogen charging until reaching the final dry nitrogen atmosphere. All the hydrogen that desorbed during the first 4 h before the assembly in the SKPFM chamber had reacted with the environmental air, therefore, the accumulation of hydrogen in the Pd layer started roughly after 4 h. The SKPFM data were analyzed using the Gwyddion software package. In order to correct increasing plane tilt in the topographical images, plane tilt corrections were carried out by a mean plane subtraction procedure setting the minimum topographical value to zero, ensuring the same contrast for all images.

### 2.5. Secondary Ion Mass Spectrometry (SIMS)

The specimen for the SIMS analysis was electrochemically charged with deuterium in 0.1 mol L<sup>-1</sup> D<sub>2</sub>SO<sub>4</sub> solution in D<sub>2</sub>O, at a cathodic current density of 10 mA cm<sup>-2</sup> for 2 h. The samples were transferred into a Cameca NanoSIMS 50 for SIMS analyses. The measurement started about 2 h after deuterium charging had finished, thus the deuterium desorbed from the surface during this time was lost. The instrument was operated with a Cs<sup>+</sup> primary ion source, having both the advantage of a small spot size (lateral resolution down to 50 nm) and the enhancement of negative secondary ion yield. The high spatial resolution is achieved by coaxial primary and secondary ion optics, which also implies that primary and secondary species need to have opposite polarity. Therefore, negative secondary ions are extracted into the double focusing mass spectrometer, consisting of an electrostatic sector combined with a magnetic sector, this combination lead to an achromatic filtering according to mass-to-charge ratio [26,27]. The hydrogen (<sup>1</sup>H = 1.0078 amu), deuterium (<sup>2</sup>D m/z = 2.0141 amu) and secondary electron maps were acquired in parallel as 256 × 256 pixel

<sup>3</sup> Etching solution: 30 ml distilled water, 5 ml nitric acid, 20 ml hydrochloric acid, 10 ml hydrogen peroxide.

images with a dwell time of 5 ms per pixel and a probe current of 1 pA. The minimum mass resolving power required to separate D from H<sub>2</sub> is 1300 which is easily reached in the NanoSIMS 50 [26]. The measurements were made such that there was no mass-interference between D and H<sub>2</sub> in the results.

## 2.6. Tensile testing

Tensile specimens with gauge dimensions of 2.0 mm width × 1.0 mm thickness × 4.0 mm length were used. Hydrogen was pre-charged into the specimens for 2 h in a 0.1 mol L<sup>-1</sup> H<sub>2</sub>SO<sub>4</sub> aqueous solution containing 3 g L<sup>-1</sup> of CH<sub>4</sub>SCN, at a cathodic current density of 10 mA cm<sup>-2</sup>. Tensile tests were carried out at an initial strain rate of 10<sup>-4</sup> s<sup>-1</sup> at room temperature with and without hydrogen pre-charging. The tensile tests were started 30 min after the hydrogen charging had finished. Deformation experiments were conducted by using a Kammrath & Weiss stage. Post-mortem microstructure characterization was performed on the fractured specimens by SE and BSE imaging to observe the deformation-induced cracks.

## 3. Results

### 3.1. Thermal Desorption Spectroscopy (TDS)

The TD analyses were performed to identify the existing trap states of hydrogen in the alloy. Fig. 3 shows the hydrogen desorption profiles at different heating rates. The curves were background corrected with respect to a non-hydrogen charged sample. The total hydrogen content in the specimens measured by TDS was ~1 wt.-ppm.

In the TD-spectra two hydrogen desorption peaks can be observed (Fig. 3). These peaks can be seen in more detail after the Gaussian peak deconvolution for each individual spectrum (Fig. 4a–e). The low temperature peak 1 indicates a weaker binding state than that of the high temperature peak 2. The temperatures of the maxima for characteristic desorption peaks ( $T_p$ ) appearing in the spectra were fitted and the shift of the peak maximum position with increasing heating rate ( $\Phi$ ) was analyzed by applying a Kissinger analysis [28] in combination with a mathematical model of the desorption process with an assumption of the first order desorption rate. Activation energies of the hydrogen desorption ( $E_a$ )

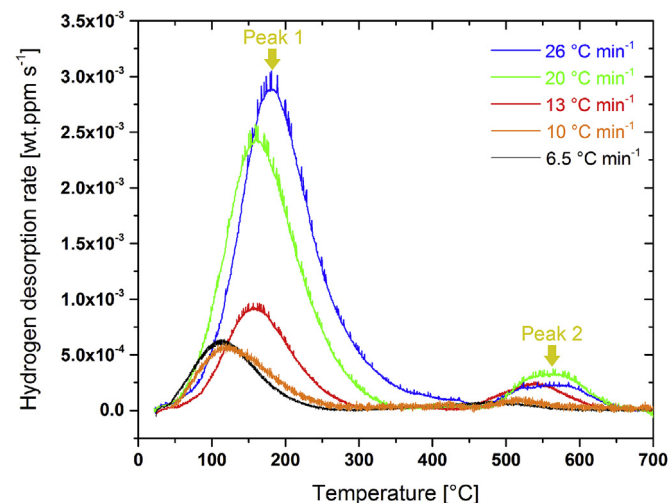


Fig. 3. Hydrogen thermal desorption spectra of Ni-22wt.-%Nb alloy at different heating rates.

were obtained from the slope of a  $\ln(\Phi \cdot T_p^2)$  vs  $T_p^{-1}$  plot [29] as a graphical solution of equation (1):

$$-\frac{E_a}{R} = \frac{\partial \ln\left(\frac{\Phi}{T_p^2}\right)}{\partial \left(\frac{1}{T_p}\right)} \quad (1)$$

The hydrogen desorption activation energy for peak 1 (low temperature peak) was found to be approx. 21 kJ mol<sup>-1</sup> and for peak 2 (high temperature peak) approx. 53 kJ mol<sup>-1</sup> (Fig. 4f and g).

TDS measurements at a constant heating rate of 26 °C min<sup>-1</sup> were performed with additional waiting time at room temperature after the end of hydrogen charging process to track the changes in the TD spectrum. Fig. 5 compares the corresponding TD curves immediately after hydrogen charging and also after 2 h and 48 h of time intervals. It was observed that after the exposure to air the intensity of peak 1 decreased, but peak 2 remained unchanged after 48 h and even its corresponding cumulative hydrogen content increased. Since the intensity of peak 1 decreased after the exposure to air, the hydrogen trapped in these sites is considered to be diffusible at room temperature. The increase in the intensity of peak 2 with time is proposed to be caused by further inward diffusion of hydrogen, leading to ongoing filling of the deeper trap sites correlated to peak 2. Note that the 2 h charging time resulted only in hydrogen loading into a thin surface layer of about 100 μm, as will be discussed in more detail further below. Also it is pointed out that peak 2 does not depend on the hydrogen activity during charging, while peak 1 does. This is why a low activity charging was chosen for the trap analysis, otherwise peak 2 would be difficult to detect.

### 3.2. Silver decoration

Ag-crystal decoration is a promising method to visualize diffusive hydrogen as a distribution of reduced silver particles and is proving to be fairly simple, fast and accurate [30–32]. Also, compared to the hydrogen microprint technique, the need for dark room procedures in the handling of the radioactive AgBr emulsions is eliminated [7].

This simple chemical method was developed by Schober and Dieker [7] and uses the special activity of atomic hydrogen on a metal surface to reduce Ag ions (Ag<sup>+</sup>) into elemental Ag (Ag<sup>0</sup>), through the reaction:



Here H<sub>ad</sub> is adsorbed atomic hydrogen on the surface.

The reduction of dissolved Ag compounds by atomic hydrogen leads to the subsequent formation of visible elemental metal crystals at surface locations of high hydrogen activity (Fig. 6) and the microstructural distribution of hydrogen fluxes can be revealed by observing the deposited crystals under SEM [7,33].

Fig. 7 shows the surface of the sample, which was immersed in the solution for 1 h without hydrogen charging. It can be seen that white silver particles (as confirmed by EDX analysis) were randomly deposited on the surface. Since nickel is chemically more active than silver, the following direct displacement reaction might take place:



This reaction may play a role in the early growth stages of the particles, which results in the deposition of silver particles of

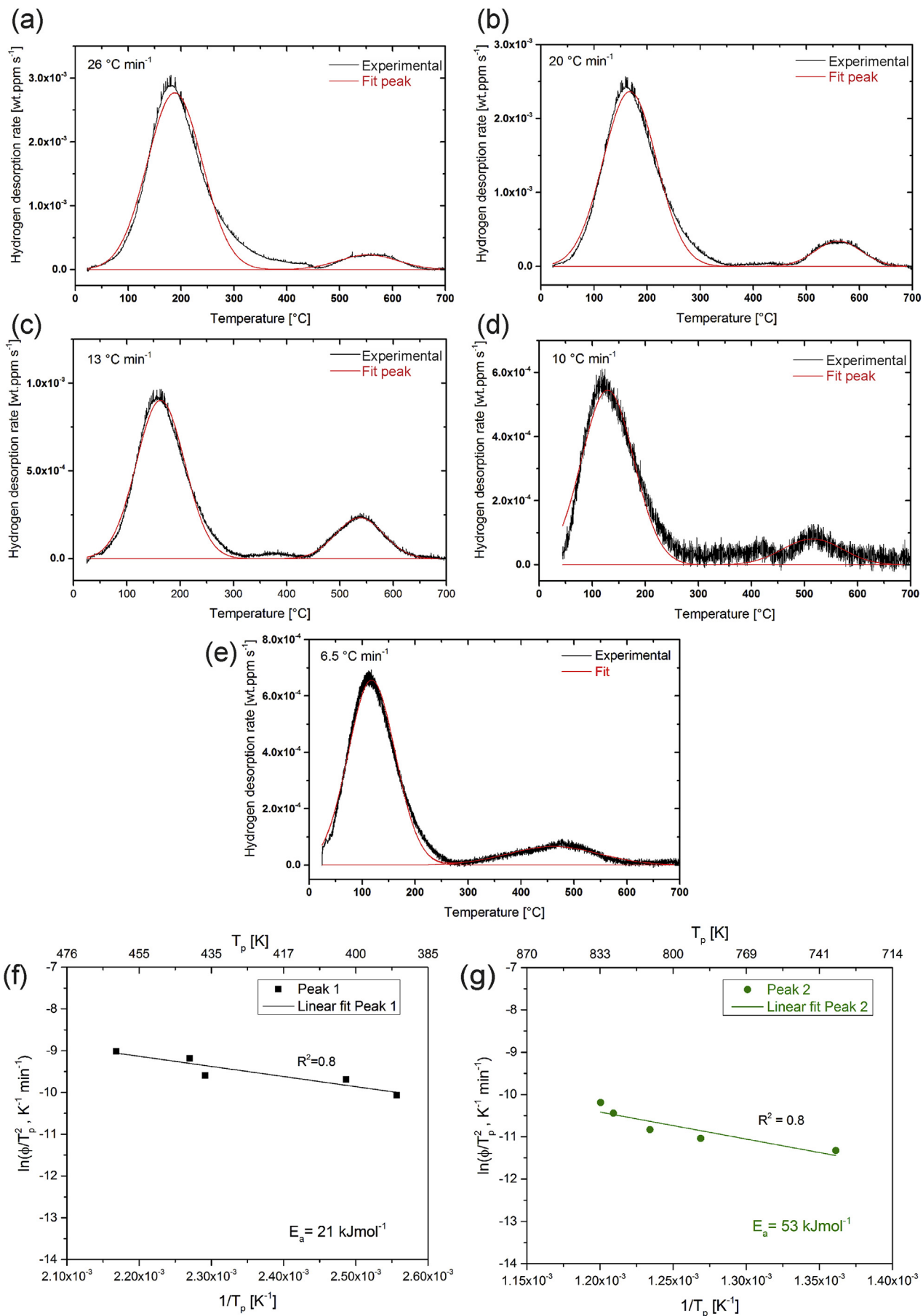


**Fig. 4.** Individual thermal desorption spectra after fitting with a Gaussian function at heating rates of: (a) 26 °C min<sup>-1</sup>, (b) 20 °C min<sup>-1</sup>, (c) 13 °C min<sup>-1</sup>, (d) 10 °C min<sup>-1</sup>, and (e) 6.5 °C min<sup>-1</sup> (f) and (g) Kissinger plots for the first and second TD-peak, respectively.

various shapes, not related to the microstructural distribution of the evading hydrogen flux [33].

Fig. 8 shows the surface of the sample which was charged with hydrogen, after immersion in the Ag decoration solution. White-colored reduced Ag particles were deposited on the  $\gamma$ -matrix, indicating a high evading hydrogen flux. EDX maps also confirmed the higher density of Ag particles on the matrix surface.

As mentioned before, the Ag reduction by Ni (reaction 3), other than the decoration reaction (Ag reduction by H, reaction 2), may occur during the reduction and deposition process. Therefore, the number of deposited silver precipitates would be larger than expected due to adsorbed hydrogen alone. On the other hand, recombination of absorbed hydrogen atoms can also take place to form  $H_2$  molecules, and this hydrogen will not be available for silver deposition. Hence, it is concluded that the silver decoration technique cannot be used quantitatively [33], but yet it provides essential qualitative and spatially resolved information about hydrogen release from the alloy directly after charging. Fig. 8 reveals that the silver crystals appear larger at the phase boundaries. However, this is not assumed to be due to a higher level of hydrogen release there, but rather to the fact that nucleation is facilitated at interfaces and that on the  $\delta$  phase no silver cations are consumed. This will be further discussed in the next section.

### 3.3. Scanning Kelvin Probe Force Microscopy (SKPFM)

Fig. 9 shows the summary of the SKPFM data taken after prolonged measuring times. The topographic images are shown in Fig. 9a–f and the corresponding potential images are presented in Fig. 9a'–f'. No changes were observed in the topographical features even after a number of successive scans over the same area for several days. The topography clearly revealed the presence of two distinct features: The dark area (with lower topography) was ascribed to the  $\gamma$ -matrix, whereas, the bright patches were intermetallic  $\delta$ -Ni<sub>3</sub>Nb phase. The height difference between the two phases was about 200 nm. The potential images presented in Fig. 9a'–f' clearly indicate the change in the contrast with time.

Since the chemical potential of hydrogen in Pd is very low, hydrogen has a strong driving force to enter the Pd layer. Hence, this layer serves as a perfect accumulation and detection layer. The observed decrease in potential is due to the formation of a hydrogen electrode on the surface of the Pd layer. This was shown and discussed in detail in [22] and [34]. Even in the dry nitrogen atmosphere, the surface of Pd is covered with an ultra-thin layer of water. When hydrogen enters the Pd, the absorbed hydrogen in Pd ( $H_{ab}$ ) is in equilibrium with hydrogen adsorbed on the surface of the Pd ( $H_{ad}$ ), at the interface between Pd and the water layer, which in turn is also in equilibrium with  $H^+$  in the ultra-thin water film. As shown in [34], the potential measured by the Kelvin probe depends on the hydrogen concentration in the Pd, following a Nernstian like behavior. Hence, we refer to the Pd surface of H containing Pd as hydrogen electrode, in the classical sense, meaning that the potential is determined by the equilibrium of  $H_{ab}/H_{ad}/H^+$ .

Since in SKPFM the tip is tapping on the surface, the work function of the tip is not stable and often conducts jumps due to contaminations. Hence, different from SKP (see Refs. [22] and [34]), the potentials measured by SKPFM are not calibrated and cannot be directly used for quantification. However, the contrast in the potential and its evolution over time provides important information about different desorption rates of hydrogen from different phases [35].

The potential profiles in Fig. 9g defined by the black line, show the evolution of potential contrast for this case. This potential contrast was the highest at about after 100 h and after that decreased with time. The difference between the average potential

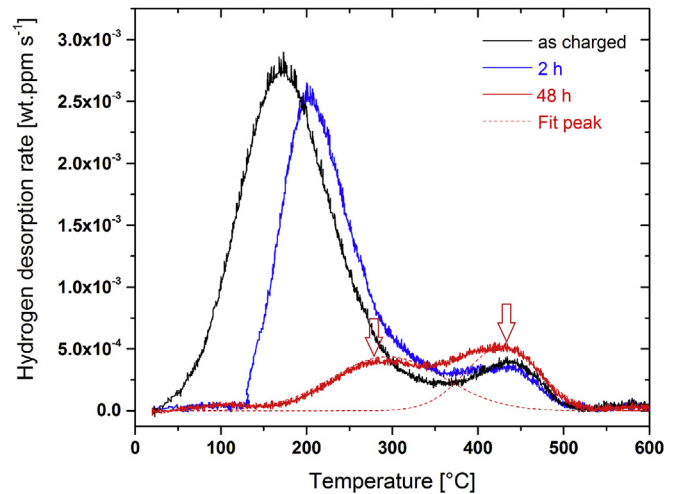


Fig. 5. Hydrogen desorption profiles of the samples measured immediately after hydrogen charging and after different air exposure times. Heating rate:  $26\text{ }^\circ\text{C min}^{-1}$

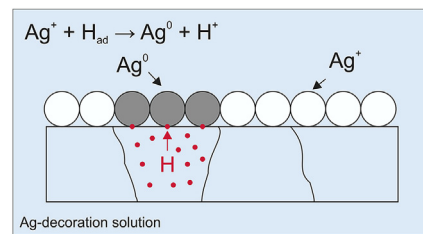


Fig. 6. Schematic principle of the Ag decoration technique.

of the  $\gamma$ -matrix and  $\delta$ -Ni<sub>3</sub>Nb is plotted in Fig. 9h. The change in the difference of the potential clearly demonstrates the enhancement and the reduction of contrast with time more clearly.

The desorption of diffusible hydrogen is a relatively fast process and difficult to detect, since there is always a lapse of about 4 h between the charging of the sample with hydrogen and reaching the optimized SKPFM measuring condition. The appearance of dark contrast in the potential images demonstrated an initially dominating release of hydrogen from the  $\gamma$ -matrix. The  $H_{ad}$  release from the  $\delta$ -Ni<sub>3</sub>Nb phase was obviously much lower. The measurement started at high potential of the H-depleted Pd layer (due to the contact with air before the assembly in the SKPFM chamber), which was the same for the entire surface, independent of the underlying phases. Thereafter the potential measured over the matrix initially dropped faster than the one measured over the  $\delta$  phase. The hydrogen release from the matrix steadily decreased, as the overall amount of hydrogen was also decreasing quickly due to the fast release rate. After about 100 h the hydrogen in the  $\gamma$ -matrix was depleted to such an extent that then the much slower release from the  $\delta$  phase became dominant. Hence, the further decrease of the potential measured on the matrix was slower than the one detected over the  $\delta$  phase, which led to a continuous reduction of the contrast (see Fig. 9h). Note that no enhanced hydrogen release at the phase boundary can be seen, as pointed out in the preceding section.

### 3.4. Secondary Ion Mass Spectrometry (SIMS)

Secondary ion mass spectrometry is a powerful analytical technique for elemental and isotopic composition analysis with very high sensitivity. SIMS is well-suited for the study of hydrogen

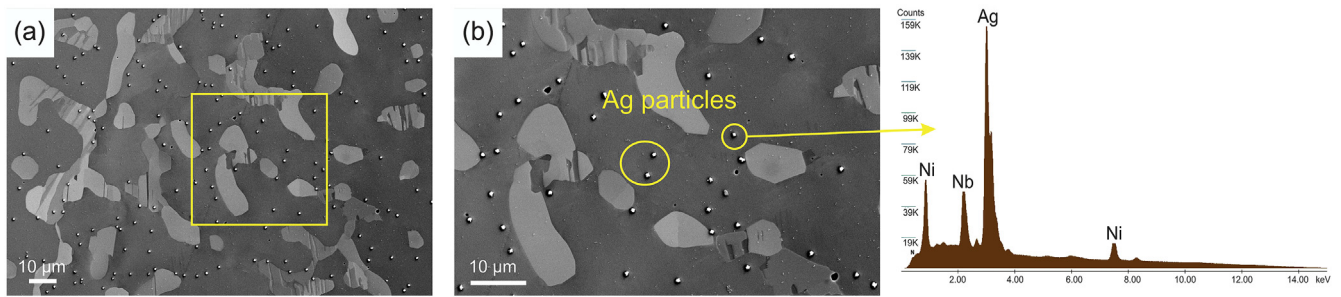


**Fig. 7.** (a) SE image of the specimen immersed in Ag decoration solution without H-charging, (b) magnified image of (a); white silver particles are distributed randomly on the surface of the H-free specimen.

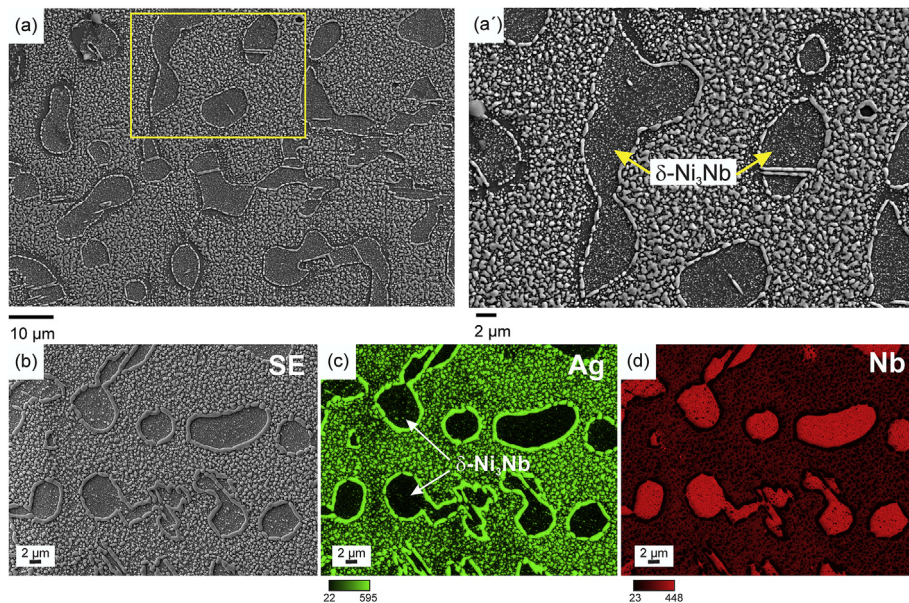


**Fig. 8.** Specimen charged with hydrogen: (a) and (a') SE images of the silver decorated surface, showing reduced Ag particles on the  $\gamma$ -matrix. (b) SE image, (c) and (d) the corresponding EDX maps of the Ag decorated surface, confirming the precipitation of the Ag particles on the  $\gamma$ -matrix, indicating the locations of the evading hydrogen flux. Each EDX map is color coded by the count frequency of the X-ray signal received by the EDX detector.

embrittlement, as the distribution of very light elements such as hydrogen and deuterium cannot be analyzed with conventional electron based techniques such as EDX. In addition, SIMS can distinguish isotopes, which is not possible with EDX. During SIMS analysis, a primary ion beam is raster scanned over the sample surface creating collision cascades inside the material, which then trigger the emission of secondary ions, electrons, and neutral particles. The secondary ions are then collected and analyzed according to their mass-to-charge ratio, thus giving important insights about the elemental and isotopic composition of the samples.

In the SIMS analysis of the current work, deuterium (D) was used as a substitute for hydrogen (H). In this way, the artefacts that could arise due to contribution from background H level are eliminated. D is an isotope of H with almost the same chemical properties as H. Furthermore, the natural abundance of D is only about 0.015%. Thus any enrichment in D above the levels of natural abundance can be unambiguously labelled and attributed to the D charging carried out in the experiment.

The intensity of secondary ion signals depends strongly on the ionization and sputtering yields, which depend on the composition (i.e. matrix effect) and crystallographic orientation of the sample, respectively. As the material was polycrystalline and had more than one phase, it is important to normalize the signal variation that

arises due to these effects so that the results can be properly interpreted. As both D and H experience the same variation as they have practically the same partial sputter yield and the same ionization probability, the D/H ratio images form a good basis for evaluating D enrichment specifically and to draw broader conclusions about the mechanisms linked to HE.

Fig. 10a–c shows an SE image and chemical maps of the hydrogen and deuterium distributions, respectively. The contrast in H distribution (Fig. 10b) indicates a weaker grain-to-grain variation (shorter range of 0–100 counts compared to the D distribution ranged 0–200 counts (Fig. 10c)). As mentioned above, in order to make SIMS imaging of H and D more directly interpretable, the variation in sputter yield has to be taken into account. A systematic correction is possible by taking the ratio of D-to-H signals (D/H) into account, enabling quantitative assessment of the local enrichment. The D/H ratio images are shown in Fig. 10d and d'. Noting that the natural abundance of D is only 0.015%, a D/H ratio of up to 3 in these images represents up to three orders of magnitude enrichment in D, thus confirming the success of electrochemical D charging. By comparing Fig. 10d with the EDX maps of Nb and Ni, Fig. 10e and f respectively, it can be seen that the areas showing less D correlates very well with the  $\delta$ -Ni<sub>3</sub>Nb phase. This suggests that the D uptake by the matrix is much more significant than by the  $\delta$ -

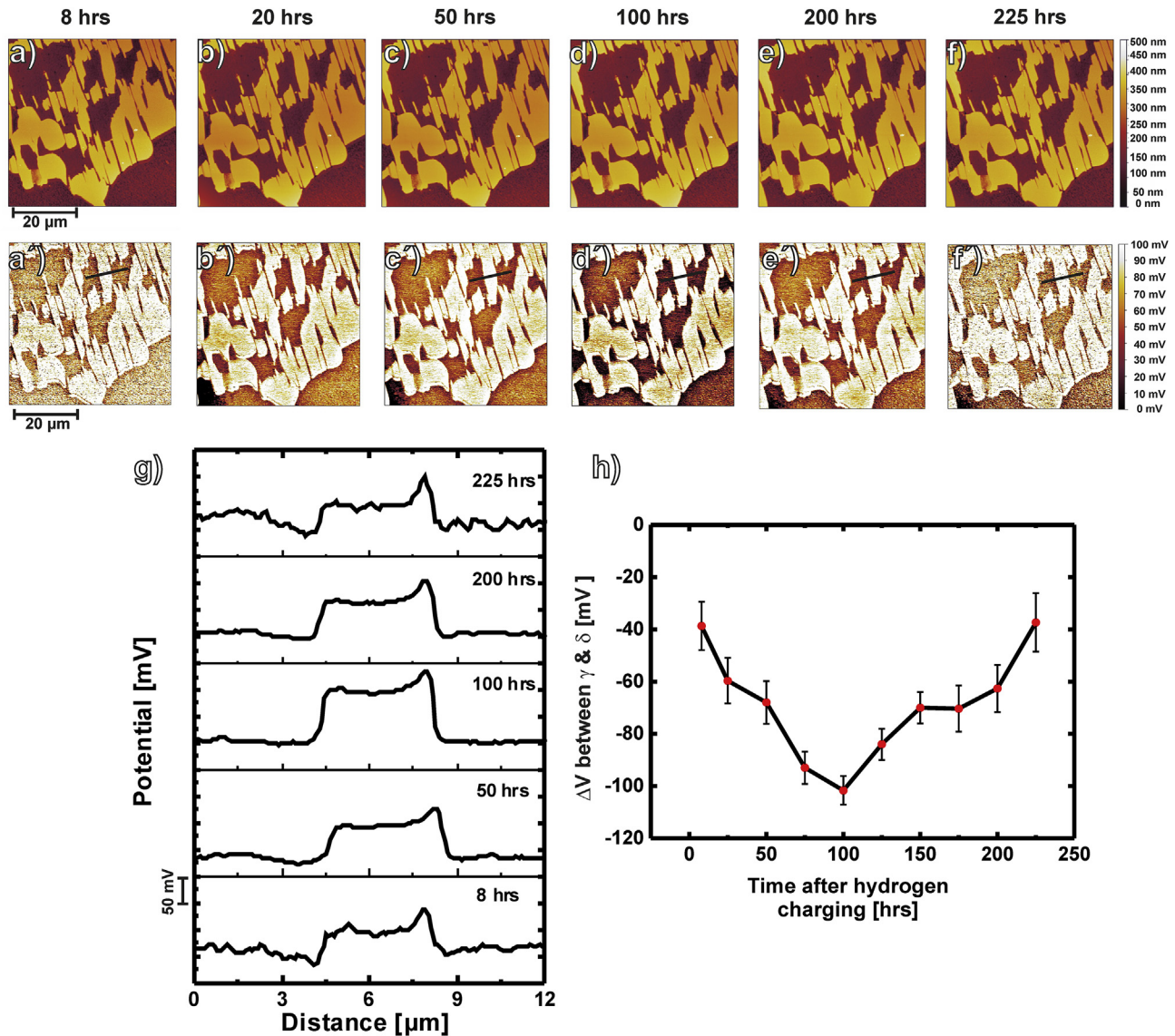


**Fig. 9.** Summary of SKPFM data obtained for Ni-22wt.-%Nb: (a)–(f) Topography maps, dark region with lower topography represents the  $\gamma$ -matrix. (a')–(f') Evolution of potential contrast on the surface over time. (g) Line profiles of surface potential along the black line shown in (a')–(f'). The potential range of each y-axis is 200 mV. (h) The change of potential difference between  $\gamma$ -matrix and  $\delta$ -Ni<sub>3</sub>Nb over time.

### Ni<sub>3</sub>Nb phase.

Note that according to Fig. 10 the deuterium intensity in the matrix is only about a factor of 3 higher than in the  $\delta$  phase, much lower than expected. However, this is a surface sensitive measurement and the deuterium depletion proceeds very fast at the surface. Hence, the measured intensities are a result of the original concentration and loss of deuterium from charging of the sample until the start of the measurement.

### 3.5. Deformation behavior in the presence of hydrogen

Since degradation of mechanical properties is a phenomenon that takes place under imposed mechanical loading, we conducted corresponding mechanical tests for correlating the hydrogen distribution in the microstructure with the resulting embrittlement behavior. Tensile testing was conducted on samples both, with and without hydrogen pre-charging to compare the deformation behavior of the material between the two states.

The fracture surface of the non-charged specimen showed

dimples as well as brittle fracture at second phases present in the microstructure (Fig. 11). Post mortem microstructural observations of the specimen deformed until fracture without hydrogen charging revealed cracking inside the  $\delta$  phase. No debonding was observed along the  $\delta$ /matrix interfaces. Fracture initiation was caused by cleavage and cracking of the intermetallic phase, which is an indication that the interfaces are not inherently brittle.

The fracture surface of the hydrogen pre-charged specimen exhibited a near surface brittle area, about 100  $\mu\text{m}$  wide (Fig. 12a), which is attributed to the hydrogen affected area. As was stated above and supported by the TDS measurements after exposure to air, only a thin surface layer was charged with hydrogen. Based on the SE images taken after fracture, this layer is assumed to be about 100  $\mu\text{m}$ . The magnified image of this brittle area showed almost featureless facets, without any dimples (Fig. 12b). This indicates that hydrogen-assisted crack propagation was caused by decohesion.

Microstructural observations of the post mortem samples showed cracks propagating along the  $\delta$ /matrix interfaces, besides

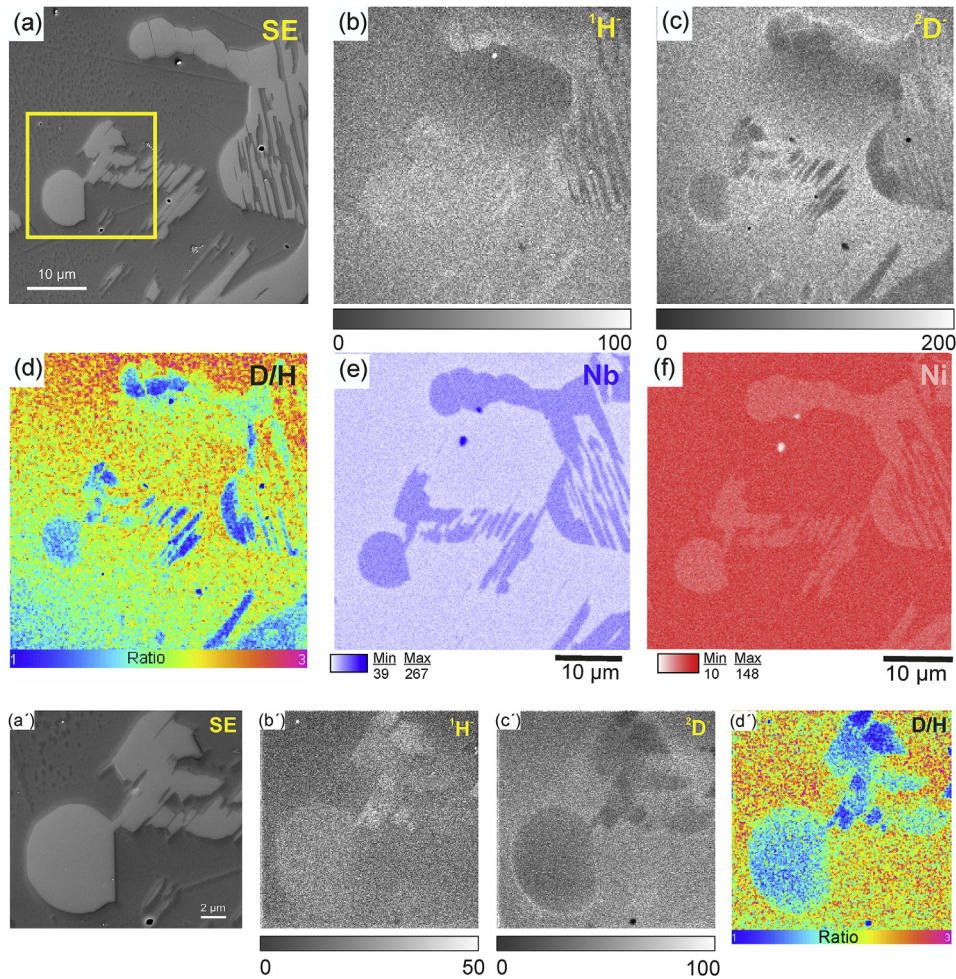


**Fig. 10.** (a) SE image and secondary ion maps of (b) H, (c) D, and (d) ( $^2\text{D}^-/{}^1\text{H}^-$ ). The field of view (FOV) in the secondary ion maps (b)–(d) is 40  $\mu\text{m}$ . (e) and (f) EDX map of Nb and Ni of the scanned area, respectively. Each EDX map is color coded by the count frequency of the X-ray signal received by the EDX detector. (a')–(d') Magnified region marked in (a). FOV in the secondary ion maps (b')–(d') is 15  $\mu\text{m}$ . The intensity scale bars shown in (b), (c), (b') and (c') indicate secondary ion counts.

$\delta$  phase cracking,  $\delta$ /matrix interface cracking associated with decohesion is considered to be the cause of the brittle fracture surfaces, observed in Fig. 12b, which is an indication that hydrogen promotes  $\delta$ /matrix decohesion.

#### 4. Discussion

Different hydrogen charging modes were used in this study. Table 2 summarizes the charging conditions and the resulting hydrogen/deuterium contents. The hydrogen contents were determined by measuring the cumulative desorbed hydrogen from room temperature up to 300  $^{\circ}\text{C}$ , corresponding to peak 1. In general, for all experiments charging in acidic environment was used, with the exception of TDS, where charging was carried out at much lower hydrogen activity from alkaline solution. Fig. 13 compares the hydrogen TD curves after charging with the conditions mentioned in Table 2, at a constant heating rate of 26  $^{\circ}\text{C min}^{-1}$ . Since the concentration of the diffusible hydrogen is proportional to the hydrogen activity during charging, charging in the acidic environment led to a high intensity of peak 1 (higher diffusible hydrogen content). A sharp peak 1 with high intensity from acidic charging makes the analysis of the other arising peaks intractable. This is the reason for choosing low activity charging for trap characterization. Comparison of the results showed that although alkaline charging

resulted in a lower hydrogen concentration, the position of the peak (temperature of desorption) remained unchanged. Also it was observed that deuterium charging used for SIMS analysis led to two TD spectra, one corresponding to deuterium (mass 4) and one to hydrogen (mass 2), although the solution contained no hydrogen. This effect occurs due to the absorption of water vapor from the air, since the charging atmosphere was not completely protected. This explains the relatively high hydrogen signal detected by SIMS (Fig. 10b and b'). It is concluded that the mode of charging in these cases caused no difference in the hydrogen trapping states, but only changed the diffusible hydrogen content.

Several techniques were employed to study the distribution and desorption behavior of hydrogen in the microstructure. As explained before each individual technique used in this study has its advantageous characteristics as well as a specific range of spatial and/or temporal resolution. Table 3 summarizes the used techniques and the corresponding information achieved from them.

As shown in Fig. 3 and Fig. 4a–e, two hydrogen desorption peaks were observed in the TD spectra at different applied heating rates, with 21  $\text{kJ mol}^{-1}$  and 53  $\text{kJ mol}^{-1}$  desorption activation energies (Fig. 4f and g). It was observed that after the exposure to air (Fig. 5) the intensity of peak 1 decreased and almost disappeared after 48 h, but peak 2 remained and even its intensity increased.

According to the Ag decoration results, desorption of diffusible

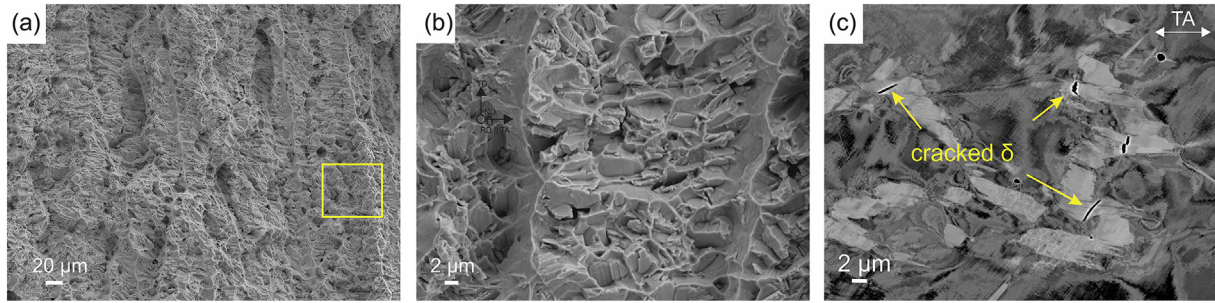


**Fig. 11.** Deformation microstructures without hydrogen charging: (a) Fracture surface, and (b) its magnified image. (c) BSE image showing the cracking of the  $\delta$  phase. (TA: Tensile Axis).

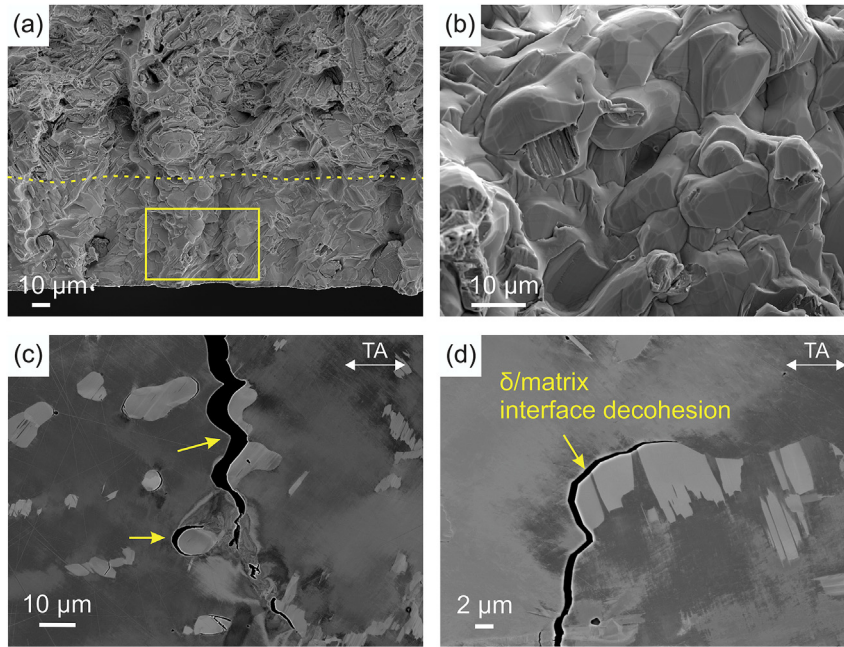


**Fig. 12.** Deformation microstructures with hydrogen pre-charging: (a) Fracture surface. The dotted yellow line indicates the boundary of the brittle surface without dimples, (b) magnified image of the marked area marked in (a). (c) and (d) BSE images showing the crack propagation along the  $\delta$ /matrix interface. (TA: Tensile Axis). (For interpretation of the references to color in this figure legend, the reader is referred to the web version of this article.)

**Table 2**

Summary of the charging conditions used in this study and comparison of the cumulative hydrogen contents corresponding to peak 1.

Mode of charging	Charging conditions (at room temperature)	Hydrogen/Deuterium content [wt.-ppm]
Acidic charging	2 h, 0.1 mol L <sup>-1</sup> H <sub>2</sub> SO <sub>4</sub> + 3 g L <sup>-1</sup> CH <sub>4</sub> N <sub>2</sub> S 10 mA cm <sup>-2</sup>	C <sub>H2</sub> = 12.94
D-charging	2 h, 0.1 mol L <sup>-1</sup> D <sub>2</sub> SO <sub>4</sub> 10 mA cm <sup>-2</sup>	C <sub>D2</sub> = 10.24 C <sub>H2</sub> = 0.91
Alkaline charging	2 h, 0.1 mol L <sup>-1</sup> NaOH -1 V (SHE)	C <sub>H2</sub> = 1.06

hydrogen at room temperature occurred from the  $\gamma$ -matrix (Fig. 8). One of the challenges in hydrogen detection experiments is the time interval between the hydrogen charging and the start of the measurements, since a certain amount of time is generally required to reach the optimal experimental conditions and the fast diffusing hydrogen (which is irrelevant for the trap analysis) is lost during this time. The advantage of Ag reduction and decoration technique is that it is relatively fast: The sample is immersed in the solution immediately after charging, revealing mainly the diffusible hydrogen flux. Irrespective of the time gap (about 4 h) between the end of hydrogen charging and the start of SKPFM measurements, the results clearly revealed preferred release of hydrogen from the  $\gamma$ -matrix until around 100 h. Hydrogen in the  $\gamma$ -matrix was

desorbed after about 100 h and then the hydrogen release was taken over by the  $\delta$  phase, which led to a continuous reduction of the contrast (Fig. 9f). Fig. 14 shows the TD spectra after acidic charging (same condition as Ag decoration and SKPFM) with additional exposure to air after H-charging. Indeed, after 96 h exposure to air the hydrogen corresponding to peak 1 was almost fully desorbed. The cumulative hydrogen content in peak 2 increased due to the hydrogen transfer from diffusible sites to deeper energy traps owing to diffusion of the hydrogen further into the bulk. After this time (96 h) the hydrogen release from the  $\delta$  phase was dominating, which is in agreement with the SKPFM results. Ag decoration after 96 h waiting time (not shown here) also revealed no silver deposition at the  $\gamma$ -matrix surface, indicating

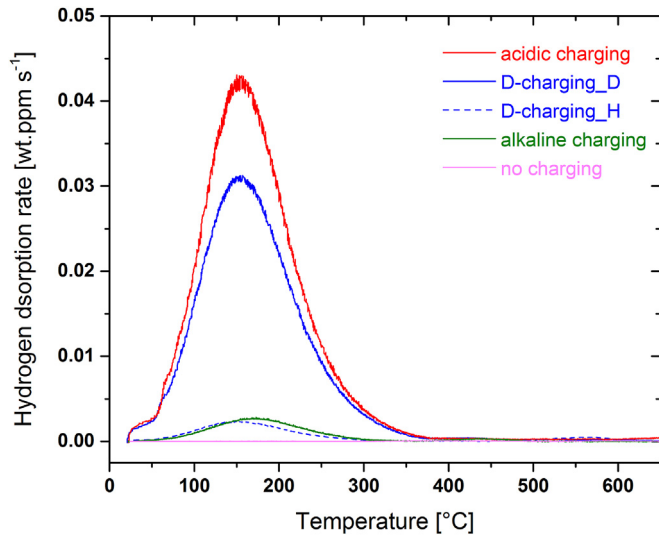


Fig. 13. Comparison of the TD curves after different charging modes (Heating rate:  $26\text{ }^{\circ}\text{C min}^{-1}$ ). More detailed information on the charging conditions is given in Table 2.

Table 3

Summary of the H-mapping techniques used in this study.

Method	Information	Spatial resolution
TDS	H trapping states/energies, respective H content	macro
Ag decoration	Diffusible H flux	mm- $\mu\text{m}$
SKPFM	Kinetics of H release from microstructure constituents	sub $\mu\text{m}$
SIMS	H distribution in the microstructure	50 nm

that the matrix was practically hydrogen depleted. The very low release rates from the  $\delta$  phase did not lead to silver deposition though, because this technique is not sensitive enough to produce a sufficient amount of reduced silver at such low hydrogen release rates.

The joint analysis of the TD results, both with and without additional exposure to air after H-charging and also the SKPFM and Ag decoration results, suggest that the first TD peak with  $21\text{ kJ mol}^{-1}$  desorption activation energy corresponds to the interstitial hydrogen in  $\gamma$ -matrix and that peak 2 with the higher desorption energy of  $53\text{ kJ mol}^{-1}$  corresponds to the  $\delta$ - $\text{Ni}_3\text{Nb}$  phase.

As explained earlier,  $\text{Ni}_3\text{Nb-DO}_a$  ( $\delta$ ) has an orthorhombic structure with eight atoms in the primitive cell ( $Pmmn$ , space group 59) and  $\text{Ni}_3\text{Nb-DO}_{22}$  ( $\gamma'$ ) has tetragonal structure ( $I4/mmm$ , space group 139). The  $\text{DO}_a$  structure is the most stable  $\text{Ni}_3\text{Nb}$  phase [36]. Conétable et al. [37] studied the hydrogen solubility in both  $\text{Ni}_3\text{Nb-DO}_a$  ( $\delta$ ) and  $\text{Ni}_3\text{Nb-DO}_{22}$  ( $\gamma'$ ) systems via Density Functional Theory (DFT) simulations. The calculations were done to reveal the bulk solubility of hydrogen in these two phases but segregation to interfaces was neglected. The  $4e$  positions (0,0.49,0.36) in  $\text{Ni}_3\text{Nb-DO}_a$  (space group 59) were found as the preferred interstitial positions for H atoms. The hydrogen solubility energy was found to be equivalent in both structures (0.19 eV) and substantially larger than in nickel (0.09 eV) [37]. Robertson [38] showed that the precipitation of the  $\gamma''$  and  $\delta$  phases induces a decrease in hydrogen solubility in alloy 718, which is consistent with the simulations that show the low solubility of hydrogen in  $\gamma''$  and  $\delta$  precipitates.

Computational studies regarding the influence of Nb atoms on the hydrogen solubility in nickel showed that when the solute Nb content increases (up to 3 at-%), the hydrogen solubility energy decreases, i.e. hydrogen solubility increases compared to pure Ni [37]. These observations underline that the solubility of hydrogen

atoms in Ni–Nb systems depends on the position and bonding state of the niobium, i.e., being either in solid solution on random substitutional positions or built into an intermetallic phase. In view of this the solubility of Ni in the  $\delta$  phase is expected to be substantially lower than in the matrix. Hence, we assume that the hydrogen released in peak 2 and which stems from the  $\delta$  phase is not the hydrogen dissolved in the  $\delta$  phase, but hydrogen bound to trapping sites, such as e.g. vacancies. This, however, requires further research.

SIMS analysis enabled the detection of the deuterium distribution in the microstructure. The results confirmed a higher deuterium content in the  $\gamma$ -matrix (Ni–Nb solid solution) and a lower content in the  $\delta$ - $\text{Ni}_3\text{Nb}$  intermetallic phase. This experimental observation agrees with the DFT results, considering the difference in hydrogen solubility energy. The corresponding desorption activation energies were identified by TDS and found to be lower in the  $\gamma$ -matrix than in the  $\delta$ - $\text{Ni}_3\text{Nb}$ , revealing that the  $\delta$  phase acts as a deeper trapping site for hydrogen. Regarding kinetics, the correlative SKPFM investigations clearly showed a faster hydrogen release rate from the  $\gamma$ -matrix compared to the  $\delta$ - $\text{Ni}_3\text{Nb}$  phase.

Deformation tests conducted on the samples containing

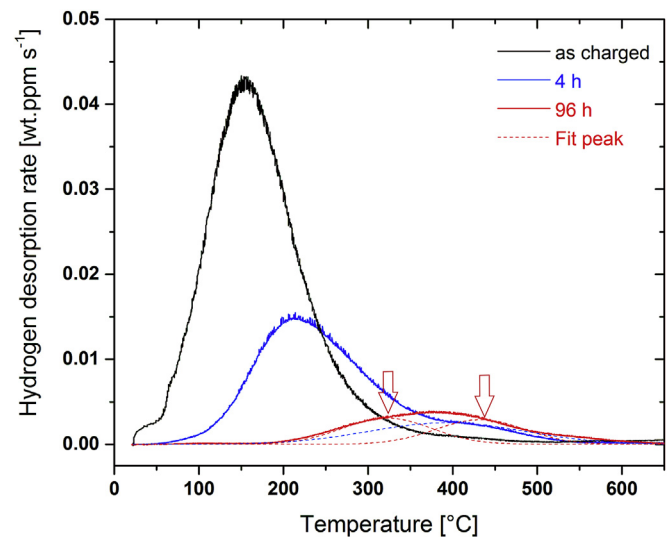


Fig. 14. Hydrogen desorption profiles of the samples measured immediately after hydrogen charging (acidic charging) and after different air exposure times (Heating rate:  $26\text{ }^{\circ}\text{C min}^{-1}$ ).

hydrogen showed that microcracks initiate and propagate at the hetero-interfaces of  $\delta$ /matrix (Fig. 12b and c), which was not the case in the uncharged samples. The depth of the area showing brittle fracture was about  $100\text{ }\mu\text{m}$  (Fig. 12a and b), which corresponds to the estimated depth of the hydrogen-affected zone. Due to the low diffusion coefficient of hydrogen in the austenitic matrix phase (of the order of  $10^{-14}\text{ m}^2\text{ s}^{-1}$  in pure nickel), 2 h of charging was not sufficient to saturate the whole thickness of the sample

(1 mm) with hydrogen. According to the fracture surfaces of the hydrogen containing samples, on the near surface area no void-like structures were found on facet surfaces, indicating interface decohesion instead of void formation as the major cause of material damage [39].

Hence, we interpret the observed hydrogen effects on cracking in the context of the hydrogen enhanced decohesion (HEDE) mechanism, which is based on the reduction in cohesive energy. Based on this model hydrogen accumulation within the lattice weakens the interatomic bonds between the metal atoms [40,41]. The decohesion hypothesis is based on charge transfer and reduction of cohesive interatomic strength so that tensile separation of atoms (decohesion) occur in preference to enhanced slip as suggested by Oriani [42,43] and others [44,45]. High concentrations of hydrogen and the associated decohesion events could occur at a variety of locations, such as at particle–matrix interfaces ahead of cracks. Decohesion could occur at or ahead of crack tips due to hydrogen trapped at these sites, and may occur as a result of bond weakening by hydrogen segregation [46–48].

The effect of the  $\delta$  phase on HE is explained as follows: As the  $\gamma$ -matrix dissolves more hydrogen than the intermetallic phase the hydrogen that evades from the  $\delta$  gets trapped at the incoherent interface between the  $\delta$  particles and the  $\gamma$ -matrix. The hydrogen desorption activation energy corresponding to this phase and/or the  $\delta$ /matrix interfaces was measured to be  $\sim 50$  kJ mol<sup>-1</sup>, indicating a rather high energy trapping site, which was demonstrated to not (or rather extremely slowly) desorb at low temperatures. The accumulated hydrogen can also seriously affect the ductility of the matrix abutting the interface. High hydrogen concentrations at particle matrix interfaces cause weakening of interatomic bonds leading to HEDE, particularly if slip planes around crack tips are not favorably oriented for slip so that elastic normal stress components can build up locally [49,50]. Microcracks can thus originate from such sites when exposed to loads (Fig. 15). When these microcracks emerge into the primary HE-induced cracks, fracture will be accelerated [51]. Due to the coarse structure of the  $\delta$  particles, the crack length at the interface is already quite large, which results in a high stress intensity in front of the crack tip. It is probable that due to the high hydrogen content dissolved in the matrix the ability of the matrix to stop the cracks formed at the interfaces by plasticity in the crack front region is reduced.

## 5. Conclusions

- (1) Multi-scale hydrogen mapping was performed with both, spatial and temporal resolution on a simple binary Ni–Nb model alloy consisting of a solid solution fcc Ni–Nb  $\gamma$ -matrix and a  $\delta$ -Ni<sub>3</sub>Nb intermetallic phase for elucidating the role of the  $\delta$  phase in hydrogen embrittlement.
- (2) Each of the experimental techniques used provide specific information of hydrogen interaction with the microstructure and a combination of these are required in order to achieve a detailed characterization of hydrogen inside complex materials.
- (3) Thermal desorption spectroscopy (TDS) reveals two hydrogen desorption peaks with desorption activation energies of 21 and 53 kJ mol<sup>-1</sup>, corresponding to H in the  $\gamma$ -matrix and  $\delta$ -Ni<sub>3</sub>Nb phase, respectively.
- (4) A silver reduction and decoration technique was used for detection of the diffusible hydrogen. Use of this method revealed the rapid and preferred desorption of diffusible hydrogen from the  $\gamma$ -matrix.
- (5) SKPFM measurements with high spatial resolution resolved the hydrogen desorption behavior from the microstructural constituents both, kinetically and with microstructural

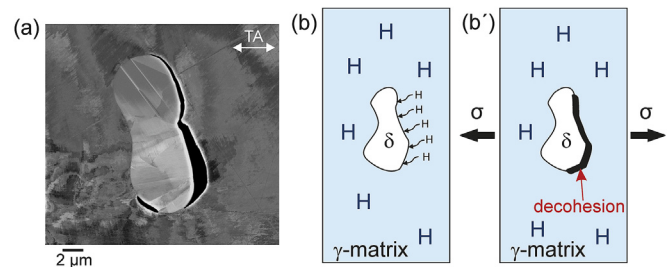


**Fig. 15.** (a) BSE image of the H-charged and deformed sample showing the crack propagation along the  $\delta$ /matrix interface (TA: Tensile Axis). (b) and (b') Schematic demonstrating the hydrogen accumulation and consequent decohesion at the  $\delta$ /matrix interface under an applied stress  $\sigma$ .

sensitivity. It was found that even after several days the matrix still shows a much higher hydrogen release rate than the  $\delta$  phase.

- (6) SIMS probing enabled the measurement of the deuterium distribution inside the microstructure, revealing higher content in the matrix, correlated with higher hydrogen solubility.
- (7) Embrittlement tests clearly revealed that the  $\delta$ /matrix interface decohesion takes place as the preferential damaging mechanism in the presence of hydrogen. Fracture facets of the hydrogen affected area showed smooth areas without dimples confirming the occurrence of decohesion.
- (8) The role of the  $\delta$ -phase in hydrogen embrittlement is explained through the accumulation of hydrogen on the  $\delta$ /matrix interfaces under applied loads, leading to the reduction of bonding strength and concurrent decohesion upon straining.

## Acknowledgments

Z. Tarzimoghadam gratefully acknowledges the support of VDM Metals GmbH, Germany. The authors are grateful for helpful discussion with J.-N. Audinot and T. Wirtz. Some of the work presented in this paper was co-funded by the National Research Funds of Luxembourg by the grant C13/MS/5951975.

## References

- [1] R.C. Reed, *The Superalloys Fundamentals and Applications*, Cambridge University Press, New York, 2006.
- [2] F. Galliano, E. Andrieu, C. Blanc, J.-M. Cloue, D. Connetable, G. Odemer, Effect of trapping and temperature on the hydrogen embrittlement susceptibility of alloy 718, *Mater. Sci. Eng. A Struct. Mater. Prop. Microstruct. Process.* 611 (2014) 370–382.
- [3] L. Liu, K. Tanaka, A. Hirose, K.F. Kobayashi, Effects of precipitation phases on the hydrogen embrittlement sensitivity of Inconel 718, *Sci. Tech. Adv. Mater* 3 (2002) 335–344.
- [4] L.F. Liu, C.Q. Zhai, C. Lu, W.J. Ding, A. Hirose, K.F. Kobayashi, Study of the effect of delta phase on hydrogen embrittlement of Inconel 718 by notch tensile tests, *Corros. Sci.* 47 (2005) 355–367.
- [5] L. Fournier, D. Delafosse, T.T. Magnin, Cathodic hydrogen embrittlement in alloy 718, *Mater. Sci. Eng. A* 269 (1999) 111–119.
- [6] A. Pundt, R. Kirchheim, Hydrogen in metals: Microstructural aspects, *Annu. Rev. Mater. Res.* 36 (2006) 555–608.
- [7] T. Schober, C. Dieker, Observation of Local Hydrogen on Nickel Surfaces, *Metall. Trans. A* 14A (1983) 2440–2442.
- [8] K. Ichitani, M. Kanno, Visualization of hydrogen diffusion in steels by high sensitivity hydrogen microprint technique, *Tech. Adv. Mater* 4 (2003) 545–551.
- [9] T.E. Perez, J. Ovejero Garcia, Direct observation of hydrogen evolution in the electron microscope scale, *Scr. Metall.* 16 (1982) 161–164.
- [10] H.K. Yalci, D.V. Edmondst, Application of the hydrogen microprint and the microautoradiography techniques to a duplex stainless steel, *Mater. Charact.* 34 (1995) 97–104.
- [11] J.P. Laurent, G. Lapasset, *Int. J. Appl. Rad. Isot* 24 (1973) 213–230.
- [12] N. Sainnier, T. Awane, J.M. Olive, S. Matsuoka, Y. Murakami, *Analyses of*

- hydrogen distribution around fatigue crack on type 304 stainless steel using secondary ion mass spectrometry, *Int. J. Hydrogen Energy* 36 (2011) 8630–8640.
- [13] K. Takai, Y. Chiba, K. Noguchi, A. Nozue, Visualization of the hydrogen desorption process from ferrite, pearlite, and graphite by secondary ion mass spectrometry, *Metal. Mater. Trans. A Phys. Metal. Mater. Sci.* 33 (2002) 2659–2665.
- [14] T. Tanaka, K. Kawakami, S.-i. Hayashi, Visualization of deuterium flux and grain boundary diffusion in duplex stainless steel and Fe–30 % Ni alloy, using secondary ion mass spectrometry equipped with a Ga focused ion beam, *J. Mater. Sci.* 49 (2013) 3928–3935.
- [15] P. Kesten, A. Pundt, G. Schmitz, M. Weisheit, H.U. Krebs, R. Kirchheim, H- and D distribution in metallic multilayers studied by 3-dimensional atom probe analysis and secondary ion mass spectrometry, *J. Alloys Compd.* 330–332 (2002) 225–228.
- [16] R. Gemma, T. Al-Kassab, R. Kirchheim, A. Pundt, Analysis of deuterium in V–Fe5at.% film by atom probe tomography (APT), *J. Alloys Compd.* 509 (2011) S872–S876.
- [17] D. Haley, S.V. Merzlikin, P. Choi, D. Raabe, Atom probe tomography observation of hydrogen in high-Mn steel and silver charged via an electrolytic route, *Int. J. Hydrogen Energy* 39 (2014) 12221–12229.
- [18] J. Takahashi, K. Kawakami, Y. Kobayashi, T. Tarui, The first direct observation of hydrogen trapping sites in TiC precipitation-hardening steel through atom probe tomography, *Scr. Mater.* 63 (2010) 261–264.
- [19] J. Takahashi, K. Kawakami, T. Tarui, Direct observation of hydrogen-trapping sites in vanadium carbide precipitation steel by atom probe tomography, *Scr. Mater.* 67 (2012) 213–216.
- [20] C. Larignon, J. Alexis, E. Andrieu, L. Lacroix, G. Odemer, C. Blanc, Investigation of Kelvin probe force microscopy efficiency for the detection of hydrogen ingress by cathodic charging in an aluminium alloy, *Scr. Mater.* 68 (2013) 479–482.
- [21] R.F. Schaller, J.R. Scully, Measurement of effective hydrogen diffusivity using the scanning Kelvin Probe, *Electrochem. Commun.* 40 (2014) 42–44.
- [22] S. Evers, C. Senöz, M. Rohwerder, Hydrogen detection in metals: a review and introduction of a Kelvin probe approach, *Sci. Tech. Adv. Mater* 14 (2013) 014201.
- [23] T. Fangt, S.J. Kennedy, L. Quan, T.J. Hickst, The structure and paramagnetism of Ni<sub>3</sub>Nb, *J. Phys. Condens. Matter* 4 (1992) 2405–2414.
- [24] M. Dehmas, J. Lacaze, A. Niang, B. Viguier, TEM study of high-temperature precipitation of delta phase in inconel 718 alloy, *Adv. Mater. Sci. Eng.* 2011 (2011) 1–9.
- [25] S.V. Merzlikin, S. Borodin, D. Vogel, M. Rohwerder, Ultra high vacuum high precision low background setup with temperature control for thermal desorption mass spectroscopy (TDA-MS) of hydrogen in metals, *Talanta* 136 (2015) 108–113.
- [26] P. Hoppe, S. Cohen, A. Meibom, NanoSIMS: Technical Aspects and Applications in Cosmochemistry and Biological Geochemistry, *Geostand. Geoanal. Res.* 37 (2013) 111–154.
- [27] L. Sangely, B. Boyer, E. de Chambost, N. Valle, J.-N. Audinot, T. Ireland, M. Wiedenbeck, J. Aleon, H. Jungnickel, J.-P. Barnes, P. Bienvenu, U. Breuer, CHAPTER 15 Secondary Ion Mass Spectrometry. Sector Field Mass Spectrometry for Elemental and Isotopic Analysis, *The Royal Society of Chemistry*, 2015, pp. 439–499.
- [28] H.E. Kissinger, Reaction kinetics in differential thermal analysis, *Anal. Chem.* 29 (1957) 1702–1706.
- [29] H.G. Lee, J.Y. Lee, Hydrogen trapping by TiC particles in iron, *Acta Metall.* 32 (1984) 131–136.
- [30] J. Ovejero-Garcia, Hydrogen microprint technique in the study of hydrogen in steels, *J. Mater. Sci.* 20 (1985) 2623–2629.
- [31] M.I. Luppó, J. Ovejero-Garcia, A new application of the hydrogen microprint technique for the study of hydrogen behaviour in steels, *J. Mater. Sci. Lett.* 14 (1995) 682–684.
- [32] A. Nagao, S. Kuramoto, K. Ichitani, M. Kanno, Visualization of hydrogen transport in high strength steels affected by stress fields and hydrogen trapping, *Scr. Mater.* 45 (2001) 1227–1232.
- [33] J. Yao, J.R. Cahoon, The use of silver decoration technique in the study of hydrogen transport in metallic materials, *Metall. Trans. A* 21 A (1990) 603–608.
- [34] S. Evers, M. Rohwerder, The hydrogen electrode in the “dry”: a Kelvin probe approach to measuring hydrogen in metals, *Electrochem. Commun.* 24 (2012) 85–88.
- [35] M. Koyama, A. Bashir, M. Rohwerder, S.V. Merzlikin, E. Akiyama, K. Tsuzaki, D. Raabe, Spatially and kinetically resolved mapping of hydrogen in a twinning-induced plasticity steel by use of scanning Kelvin probe force microscopy, *J. Electrochem. Soc.* 162 (2015) C638–C647.
- [36] J.W. Brooks, P.J. Bridges, Metallurgical stability of Inconel 718, in: D.N. Duhl, G. Maurer, S. Antolovich, C. Lund, S. Reichman (Eds.), *Superalloys 1988* (Warrendale, PA: the Metallurgical Society, 1988), 1988, pp. 33–42.
- [37] D. Connétable, F. Galliano, G. Odemer, C. Blanc, É. Andrieu, DFT study of the solubility of hydrogen and carbon in Ni<sub>3</sub>Nb-D0a and Ni<sub>3</sub>Nb-D022 systems, *J. Alloys Compd.* 610 (2014) 347–351.
- [38] W.M. Robertson, Hydrogen Permeation and Diffusion in Inconel 718 and Incoloy 903, *Metall. Trans. A* 8A (1977) 1709–1712.
- [39] R.P. Gangloff, Hydrogen assisted cracking of high strength alloys, *Comprehensive structural integrity*, in: I. Milne, R.O. Ritchie, B. Karihaloo (Eds.), *Environmentally Assisted Fracture*, 6, Elsevier, 2003, pp. 31–101.
- [40] L.B. Pfeil, The effect of occluded hydrogen on the tensile strength of iron, *Proc. Roy. Soc. Lond. A* 112 (1926) 128–195.
- [41] A.R. Troiano, The role of hydrogen and other interstitials in the mechanical behavior of metals, *Trans. ASM* 52 (1960) 54–80.
- [42] R.A. Oriani, A mechanistic theory of hydrogen embrittlement of steels, *Ber. Bunsenges. Phys. Chem.* 76 (1972) 848–857.
- [43] R.A. Oriani, P. Josephic, Equilibrium aspects of hydrogen-induced cracking of steels, *Acta Metall.* 22 (1974) 1065–1074.
- [44] W.W. Gerberich, P.G. Marsh, J.W. Hoehn, Hydrogen induced cracking mechanisms – Are there critical experiments?, in: A.W. Thompson, N.R. Moody (Eds.), *Hydrogen Eff. Mater.* (1996) 539–553.
- [45] C.J. McMahon, Hydrogen-induced intergranular fracture of steels, *Eng. Fract. Mech.* 68 (2001) 773–788.
- [46] R. Kirchheim, Reducing grain boundary, dislocation line and vacancy formation energies by solute segregation. I. Theoretical background, *Acta Mater.* 55 (2007) 5129–5138.
- [47] R. Kirchheim, Reducing grain boundary, dislocation line and vacancy formation energies by solute segregation II. Experimental evidence and consequences, *Acta Mater.* 55 (2007) 5139–5148.
- [48] R. Kirchheim, On the solute-defect interaction in the framework of a defactant concept, *Int. J. Mater. Res.* 100 (2009) 483–487.
- [49] Y. Liang, P. Sofronis, Toward a phenomenological description of hydrogen-induced decohesion at particle/matrix interfaces, *J. Mech. Phys. Solids* 51 (2003) 1509–1531.
- [50] Y. Liang, P. Sofronis, Micromechanics and numerical modelling of the hydrogen-particle-matrix interactions in nickel-base alloys, *Model. Simul. Mater. Sci. Eng.* 11 (2003) 523–551.
- [51] S. Lynch, Hydrogen embrittlement phenomena and mechanisms, *Corros. Rev.* 30 (2012).